

The Lifecycle of Semidiurnal Internal Tides over the Northern Mid-Atlantic Ridge

CLÉMENT VIC AND ALBERTO C. NAVEIRA GARABATO

University of Southampton, National Oceanography Centre, Southampton, United Kingdom

J. A. MATTIAS GREEN

School of Ocean Sciences, Bangor University, Menai Bridge, United Kingdom

CARL SPINGYS AND ALEXANDER FORRYAN

University of Southampton, National Oceanography Centre, Southampton, United Kingdom

ZHONGXIANG ZHAO

Applied Physics Laboratory, University of Washington, Seattle, Washington

JONATHAN SHARPES

School of Environmental Sciences, University of Liverpool, Liverpool, United Kingdom

(Manuscript received 20 June 2017, in final form 27 September 2017)

ABSTRACT

The life cycle of semidiurnal internal tides over the Mid-Atlantic Ridge (MAR) sector south of the Azores is investigated using in situ, a high-resolution mooring and microstructure profiler, and satellite data, in combination with a theoretical model of barotropic-to-baroclinic tidal energy conversion. The mooring analysis reveals that the internal tide horizontal energy flux is dominated by mode 1 and that energy density is more distributed among modes 1–10. Most modes are compatible with an interpretation in terms of standing internal tides, suggesting that they result from interactions between waves generated over the MAR. Internal tide energy is thus concentrated above the ridge and is eventually available for local diapycnal mixing, as endorsed by the elevated rates of turbulent energy dissipation ϵ estimated from microstructure measurements. A spring–neap modulation of energy density on the MAR is found to originate from the remote generation and radiation of strong mode-1 internal tides from the Atlantis-Meteor Seamount Complex. Similar fortnightly variability of a factor of 2 is observed in ϵ , but this signal's origin cannot be determined unambiguously. A regional tidal energy budget highlights the significance of high-mode generation, with 81% of the energy lost by the barotropic tide being converted into modes >1 and only 9% into mode 1. This has important implications for the fraction (q) of local dissipation to the total energy conversion, which is regionally estimated to be ~ 0.5 . This result is in stark contrast with the Hawaiian Ridge system, where the radiation of mode-1 internal tides accounts for 30% of the regional energy conversion, and $q < 0.25$.

1. Introduction

Understanding what sets the strength and geographical variability of oceanic diapycnal mixing is a critical issue in physical oceanography because of the central role that turbulent mixing processes play in the oceanic meridional overturning circulation and its impact on climate (e.g., Munk and Wunsch 1998). A large fraction of the energy available for diapycnal mixing is

provided by the tides (Wunsch and Ferrari 2004), with satellite measurements indicating that the semidiurnal M_2 barotropic tide dissipates one-third of its energy in the deep ocean globally (Egbert and Ray 2000, 2001). This dissipation is localized to specific hot spots in which enhanced tidally driven turbulent dissipation is revealed by in situ measurements, mostly over midocean ridges (Polzin et al. 1997; Rudnick et al. 2003) and near isolated seamounts (Lueck and Mudge 1997). The route to dissipation of the barotropic tide in the deep ocean primarily involves a conversion into baroclinic tides, that is,

Corresponding author: Clément Vic, c.vic@soton.ac.uk

internal waves with tidal frequencies. Internal tides form a reservoir of turbulent energy, the dissipation of which results in irreversible diapycnal mixing. The fate of this reservoir—mainly, where and how internal waves break—is poorly understood on a global scale, yet is of key importance in setting the geography of diapycnal mixing (MacKinnon et al. 2017). Diapycnal mixing is heterogeneous and strongly impacts the distributions of tracers and water masses (Armi 1979) and the intensity and structure of the overturning circulation (Mashayek et al. 2015; de Lavergne et al. 2016).

This paper addresses the life cycle—from generation to dissipation—of semidiurnal internal tides over the Mid-Atlantic Ridge (MAR) sector south of the Azores by combining a theoretical model with multisource in situ and satellite data. Our primary goals are to document the key stages of the internal tides' life cycle and to outline the energy budget of the internal tides in the region. The northern MAR is a relatively unexplored source of internal tides compared to the more widely studied Hawaiian Ridge system [as part of the Hawaiian Ocean Mixing Experiment (HOME; e.g., Rudnick et al. 2003)] and the southern MAR [under the auspices of the Brazil Basin Tracer Release Experiment (BBTRE; Polzin et al. 1997; Ledwell et al. 2000)]. However, recent theoretical (Melet et al. 2013; Lefauve et al. 2015) and numerical (Timko et al. 2017) modeling studies suggest that the northern MAR is an important site for internal tide generation and dissipation and, as such, provides an interesting point of contrast to the Hawaiian Ridge and southern MAR.

The work presented here is part of the RidgeMix project, which seeks to understand and quantify the upward supply of nutrients to the upper layers of the North Atlantic Subtropical Gyre. As part of RidgeMix, a mooring was deployed on the edge of the MAR, designed to resolve variability in velocity and temperature at tidal and higher frequencies throughout the entire water column with high vertical resolution. This mooring provides data with which local internal tide dynamics may be described for up to 10 baroclinic modes. In addition, direct measurements of turbulent energy dissipation from microstructure profilers were obtained above the MAR to assess the rate of dissipation of internal tides. Application of a 2D spectral model of barotropic-to-baroclinic energy conversion (St. Laurent and Garrett 2002) and analyses of tidal model estimates of barotropic tidal dissipation (Egbert and Ray 2000) and satellite altimetry-derived mode-1 horizontal energy flux data (Zhao et al. 2016) allow us to extend our understanding of the internal tides' life cycle to a regional scale.

In sections 2 and 3, we introduce the data and methods used in this study, respectively. The characteristics of semidiurnal internal tides, characterized with a combination of a theoretical model, mooring data, and microstructure measurements, are presented in section 4. Our regional perspective of tidal energy conversion and dissipation is discussed in section 5. Our main conclusions are drawn in section 6.

2. Data

In this section, we briefly describe in situ data collection conducted during the RidgeMix cruise (Sharples 2016). We then document the global gridded datasets that we use to compute tidal energy-related quantities on a regional scale (section 3).

a. RidgeMix data

1) MOORING DATA

A mooring was deployed at 36.23°N, 32.75°W (Fig. 1a) on 26 September 2015 and recovered on 4 July 2016. It was equipped with 41 RBR self-logging thermistors, two Teledyne RD Instruments (TRDI) 75-kHz-long Ranger acoustic Doppler current profilers (ADCPs), and two Flowquest 75-kHz ADCPs. The positioning of thermistors and ADCPs along the mooring line is shown in Fig. 1b. The 36 thermistors monitored temperature with a sampling period of 15 s during the whole mooring deployment, whereas 5 thermistors stopped recording between a few days and a month after deployment. The spacing between thermistors was reduced where the stratification is maximum in order to capture high (up to 10) dynamical modes [section 3 and Fig. 2 (below)]. The ADCPs recorded hourly averaged horizontal velocity (over 50 and 150 pings for the TRDI and Flowquest ADCPs, respectively) with 8-m vertical bins. Their positioning allowed sampling of the entire water column down to ~100 m above the seafloor.

2) MICROSTRUCTURE DATA

The rate of turbulent energy dissipation ε was determined directly using vertical microstructure profilers (VMPs). We deployed free-falling Rockland Scientific International¹ (RSI) VMP-6000 instruments at stations on and off the ridge (see Fig. 1a for locations). A tethered RSI VMP-2000 instrument was deployed continuously during 25-h stations (thus sampling two semidiurnal tidal cycles) in the vicinity

¹ <http://rocklandsscientific.com>

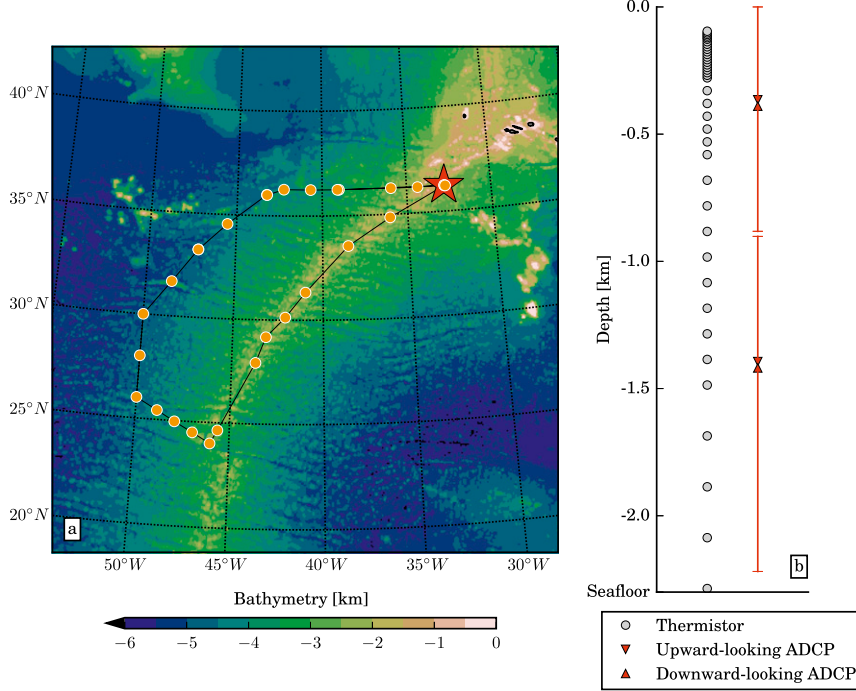


FIG. 1. (a) RidgeMix experiment location. Background shading indicates bathymetry, orange circles are VMP stations, and the red star is the mooring location. (b) Mooring sketch; gray dots are thermistors, red triangles are ADCPs, and red segments are ADCP ranges.

of the mooring location during spring and neap tides (6 and 28 June 2016, respectively). VMPs record velocity shear $\partial u / \partial z$ and temperature variance at centimeter scales. Assuming isotropy, the rate of turbulent energy dissipation is given by $\varepsilon = 15\nu/2(\partial u / \partial z)^2$ (W kg^{-1}), where ν is the molecular viscosity of seawater (Oakey 1982). To compare dissipation with model estimates of energy conversion, we compute the depth-integrated dissipation (W m^{-2}) between 50 m and the seafloor:

$$\varepsilon_z = \int_{-H}^{-50\text{m}} \rho_0 \varepsilon dz, \quad (1)$$

where H is the local depth, and ρ_0 is the mean density of the profile. We did not include the uppermost 50 m, where mixed layer processes are expected to dominate compared to internal tide breaking.

b. Global gridded datasets

1) SRTM30_PLUS

The Shuttle Radar Topography Mission dataset (SRTM30_PLUS; Becker et al. 2009) is a global bathymetry dataset at a 30-s resolution. SRTM30_PLUS is based on the 1-min Smith and Sandwell (1997) bathymetry and incorporates higher-resolution data from

ship soundings wherever available. The MAR sector south of the Azores has been intensively surveyed (see Fig. 3 in Timko et al. 2017), and SRTM30_PLUS is significantly enriched by small-scale topographic features compared to the Smith and Sandwell (1997) dataset.

2) WOA13

Temperature and salinity data required to compute the buoyancy frequency are from the 1°-resolution *World Ocean Atlas 2013 (WOA13)* version 2 climatology² (Locarnini et al. 2013; Zweng et al. 2013). This climatology is computed by objective analysis of historical hydrographic profiles from many different sources.

3) TPXO

Barotropic tide currents (amplitude and phase) were extracted from the 1/12°-resolution inverse tidal model for the Atlantic Ocean, the TPXO AO_ATLAS,³ a regional version of TPXO8 (Egbert and Erofeeva 2002). We hereinafter refer to this dataset as TPXO.

² <https://www.nodc.noaa.gov/OC5/woa13/>

³ <http://volkov.oce.orst.edu/tides/AO.html>

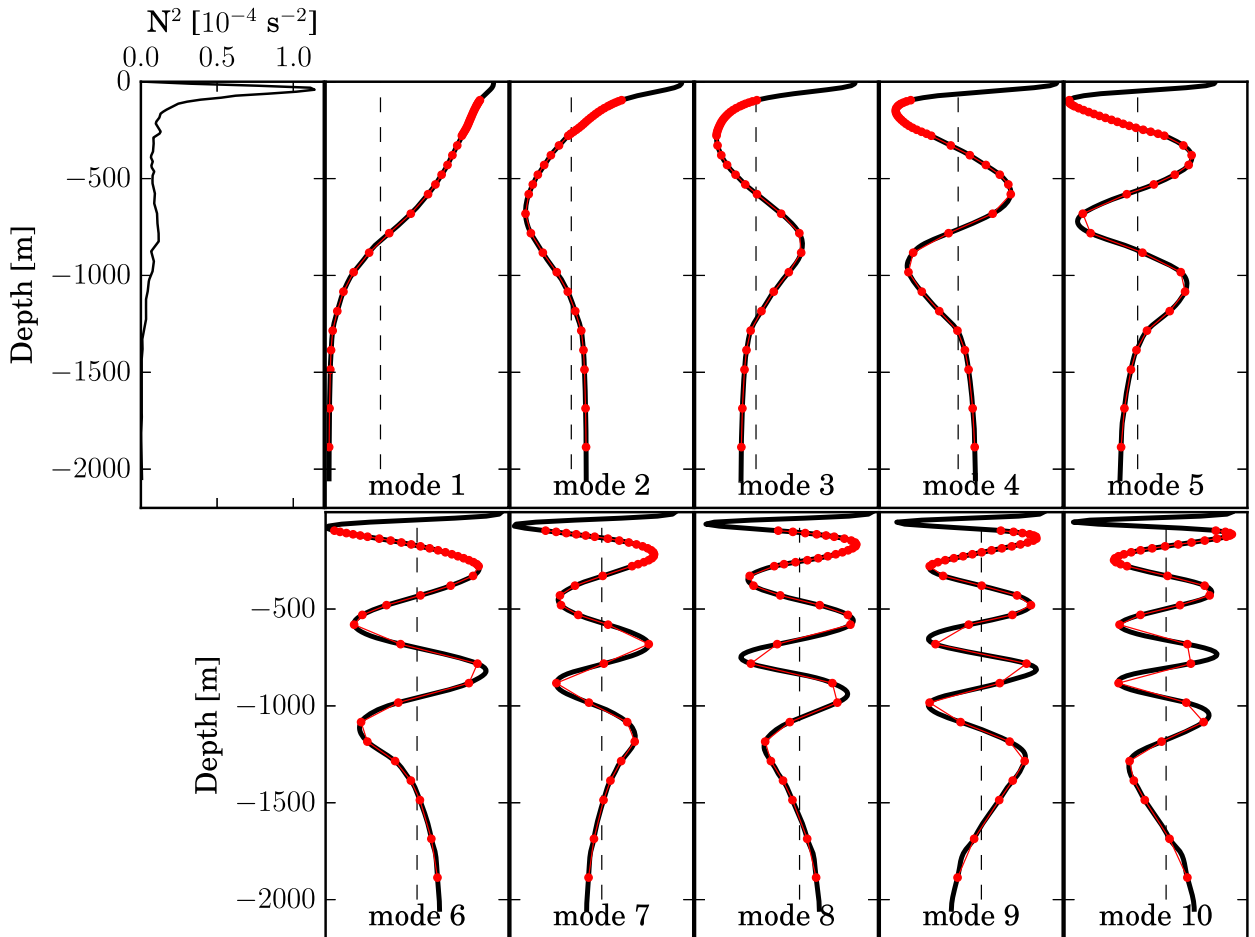


FIG. 2. Mean stratification N^2 and first 10 baroclinic modes Π_n for pressure and horizontal velocity. Vertical dashed lines represent $x = 0$ and x axes are normalized. Red dots are the positions of thermistors, and red lines are linearly interpolated between them.

4) MODE-1 M₂ ENERGY FLUXES AND SEA SURFACE HEIGHT FROM SATELLITE ALTIMETRY

Mode-1 M₂ internal tide horizontal energy flux and sea surface height (SSH) data at a horizontal resolution of 1/5° from Zhao et al. (2016) were used in this study to quantify the propagation of baroclinic tidal energy on a regional scale. Zhao et al. (2016) use a two-dimensional plane wave fit method to extract internal tides from satellite SSH and apply a modal decomposition that allows the inference of mode-1 internal tide pressure from SSH. Assuming that the energy partition between potential and kinetic energy components depends only on latitude and tidal frequency, the internal tide velocity is also estimated from SSH. Finally, vertically integrated horizontal energy fluxes \mathbf{F}_s^1 are computed (appendix A in Zhao et al. 2016). Positive divergence of the horizontal energy flux, hereinafter denoted $(\nabla \cdot \mathbf{F}_s^1)^+$, indicates regions of mode-1 internal tide generation.

3. Methods

In this section, we outline the methodology used in this study. First, we implement a theoretical model for the generation of internal tides (section 3a). This is followed with an analysis of mooring data to characterize internal tide properties (section 3b). Finally, we estimate the barotropic tidal energy loss on a regional scale from a tidal model (section 3c).

a. Theoretical model of barotropic-to-baroclinic energy conversion

In a stratified fluid, the interaction of a current with varying topography generates internal waves. Under different sets of flow characteristics and dynamical assumptions, models and parameterizations for internal wave generation have been developed (e.g., Baines 1998; Nycander 2005). When the current of interest is the barotropic tide, two dimensionless parameters mainly govern the nature of internal waves (St. Laurent

and Garrett 2002; Garrett and Kunze 2007): the ratio of topographic slope $s = \nabla h$ to wave characteristic slope $\alpha = \sqrt{(\omega^2 - f^2)/(N^2 - \omega^2)}$ and the ratio of tidal excursion to topographic length scale ku_0/ω , where u_0 is the barotropic tidal velocity and k is the topographic horizontal wavenumber. In the deep ocean—that is, far from continental shelves and slopes—the major topographic features responsible for barotropic tidal dissipation are midocean ridges (Egbert and Ray 2000, 2001). Over these ridges, topographic slopes are dominantly subcritical ($s/\alpha < 1$) and tidal excursions are smaller than topographic scales ($ku_0/\omega < 1$) because of weak barotropic tidal currents [$u_0 = O(1) \text{ cm s}^{-1}$]. Most deep-ocean barotropic-to-baroclinic energy conversion models are based on these two assumptions, which permit the derivation of linear equations (e.g., Bell 1975a,b; Jayne and St. Laurent 2001; Llewellyn Smith and Young 2002; St. Laurent and Garrett 2002; Nycander 2005).

Among the various existing models, we chose to use a two-dimensional spectral model that follows St. Laurent and Garrett (2002). Although computationally more expensive, this method offers an extensive characterization of the vertical energy flux, providing information such as modal content and flux direction. The barotropic-to-baroclinic vertical energy flux E_f [see Eq. (10) in St. Laurent and Garrett (2002)] may be estimated as

$$E_f(K, \theta) = \frac{1}{2} \rho_0 \frac{[(N_b^2 - \omega^2)(\omega^2 - f^2)]^{1/2}}{\omega} (u_e^2 \cos^2 \theta + v_e^2 \sin^2 \theta) K \phi(K, \theta) [\text{W m}^{-2} (\text{rad m}^{-1})^{-2}], \quad (2)$$

where N_b is the buoyancy frequency close to the bottom computed from WOA13; u_e (v_e) is the barotropic tidal velocity amplitude from TPXO in the direction of the semimajor (semiminor) axis of the tidal ellipse [(x_e, y_e) coordinate system]; $K = (k_x^2 + k_y^2)^{1/2}$ is the total horizontal wavenumber, with k_x and k_y being the horizontal wavenumbers in the (x_e, y_e) coordinate system; and $\theta = \arctan(k_y/k_x)$. The 2D power spectrum of topography ϕ is normalized to satisfy $\int_0^{2\pi} \int_0^\infty \phi(K, \theta) K dK d\theta = \bar{h}^2$, where \bar{h}^2 is the mean square height of topography.

From Eq. (2), we define the azimuthally averaged vertical energy flux as

$$E_f^a(K) = \frac{1}{2\pi} \int_0^{2\pi} E_f(K, \theta) K d\theta [\text{W m}^{-2} (\text{rad m}^{-1})^{-2}], \quad (3)$$

and the radially integrated vertical energy flux as

$$E_f^r(\theta) = \int_{K_1}^\infty E_f(K, \theta) dK [\text{W m}^{-2} (\text{rad m}^{-1})^{-2}]. \quad (4)$$

The total vertical energy flux is

$$E_f^t = \int_0^{2\pi} \int_{K_1}^\infty E_f(K, \theta) K dK d\theta (\text{W m}^{-2}), \quad (5)$$

where the lower boundary of integration in wavenumber space is the mode-1 equivalent wavenumber K_1 to take into account the finite depth of the ocean (Llewellyn Smith and Young 2002). We also define the vertical energy flux into mode j as

$$E_f^j = \int_0^{2\pi} \int_{K_j - \delta K/2}^{K_j + \delta K/2} E_f(K, \theta) K dK d\theta (\text{W m}^{-2}), \quad (6)$$

where $\delta K = K_2 - K_1$, and the equivalent wavenumber of mode j is

$$K_j = \frac{j\pi(\omega^2 - f^2)^{1/2}}{N_0 b}. \quad (7)$$

The quantities N_0 and b are parameters of an exponential fit to the buoyancy frequency $N = N_0 \exp(z/b)$ (St. Laurent and Garrett 2002).

b. Energy density and horizontal energy flux from mooring data

Internal tide energy density E and horizontal energy flux \mathbf{F} are estimated from mooring data following Nash et al. (2005). Here, we briefly recall the main steps of their procedure.

The wave velocity $\mathbf{u}'(z, t)$ is defined as

$$\mathbf{u}'(z, t) = \mathbf{u}(z, t) - \bar{\mathbf{u}}(z) - \bar{\mathbf{u}}_0(t), \quad (8)$$

where $\mathbf{u}(z, t)$ is the instantaneous velocity as recorded by the instrument, $\bar{\mathbf{u}}(z)$ is the time mean of that velocity, and $\bar{\mathbf{u}}_0(t)$ is defined by the baroclinicity condition $(1/H) \int_{-H}^0 \mathbf{u}'(z, t) dz = 0$. Here, the time-mean velocity is defined as the 5-day running mean (as in Zhao et al. 2010) to filter out meso- to submesoscale processes (at least below the surface mixed layer). Sensitivity on the length of the time window has been tested and found to be weak as the signals are further bandpassed filtered in the semidiurnal wave band.

The wave pressure $p'(z, t)$ is defined as

$$p'(z, t) = p_{\text{surf}}(t) + \int_z^0 \rho'(\hat{z}, t) g d\hat{z}, \quad (9)$$

where p_{surf} is the surface pressure, g is the acceleration of gravity, and ρ' is the density perturbation associated with the wave. Although p_{surf} is not measured, $p'(z, t)$ is constrained by the baroclinicity

condition $(1/H) \int_{-H}^0 p'(z, t) dz = 0$. Formally, the density perturbation ρ' is defined as

$$\rho'(z, t) = \rho(z, t) - \bar{\rho}(z), \quad (10)$$

where $\rho(z, t)$ is the instantaneously measured density and $\bar{\rho}(z)$ is the time-mean vertical density profile. Since the mooring is only equipped with thermistors, we cannot derive the density directly. As an alternative, $\rho'(z, t)$ is inferred from the vertical displacement of isopycnals $\xi(z, t)$ (approximated as isotherms here) relative to their mean position:

$$\rho'(z, t) = [\bar{\rho}(z)/g] \bar{N}^2(z) \xi(z, t), \quad (11)$$

where $\bar{N}^2(z) = -(g/\rho_0) \partial_z \bar{\rho}$ is the time-mean buoyancy frequency profile computed from *WOA13* temperature and salinity interpolated to the mooring position. The linear relationship between ρ' and ξ is valid because of the slowly varying profile of time-mean density with depth (Desaubies and Gregg 1981). The vertical displacement of isopycnals $\xi(z, t)$ is given by

$$\xi(z, t) = T'(z, t) [\partial_z \bar{T}(z)]^{-1}, \quad (12)$$

where $T'(z, t) = T(z, t) - \bar{T}(z)$ is the temperature anomaly relative to a 5-day running mean, and $\partial_z \bar{T}(z)$ is the time-mean vertical gradient of temperature (e.g., Alford 2003). We checked that $\partial_z \bar{T}(z)$ close to the bottom was bounded by a lower value ($9 \times 10^{-4} \text{ }^\circ\text{C m}^{-1}$) representative of a stratified environment and that would not lead to singularities in Eq. (12).

The variables \mathbf{u}' , p' , and ξ are then filtered at the M_2 frequency ω using a bandpass fourth-order Butterworth filter in the bandwidth $\{c^{-1}\omega, c\omega\}$ with $c = 1.25$ (Alford 2003; Alford and Zhao 2007a; Zhao et al. 2010). We ensured that at the mooring latitude the value of c does not lead to overlapping of the wave band with the near-inertial band $\{c^{-1}f, cf\}$, where f is the Coriolis frequency. However, semidiurnal frequencies M_2 and S_2 are too close to be adequately resolved by a bandpass filtering method. The filtered variables thus contain both M_2 and S_2 and hence display spring–neap variability.

Variables are next projected onto baroclinic modes. The baroclinic modes for vertical displacement $\Phi_n(z)$ ($n > 0$) are defined as the solutions of the eigenvalue problem

$$\frac{d^2 \Phi_n}{dz^2} + \frac{N^2(z)}{c_n^2} \Phi_n(z) = 0, \quad (13)$$

with boundary conditions $\Phi_n(0) = \Phi_n(-H) = 0$, where n is the mode number and c_n is its eigenspeed (Gill 1982), defined as

$$c_n = \frac{H}{n\pi} \int_{-H}^0 N(z) dz. \quad (14)$$

The corresponding modes for pressure and horizontal velocity $\Pi_n(z)$ are defined as

$$\Pi_n(z) = \rho_0 c_n^2 \frac{d\Phi_n}{dz}. \quad (15)$$

The buoyancy frequency $N(z)$, computed from *WOA13*, and the corresponding modes $\Pi_n(z)$ for $n = 1, \dots, 10$ are shown in Fig. 2. The modes as observed by the array of thermistors are superimposed in red. Projection of variables onto these modes—for example, for velocity $\mathbf{u}'(z, t) = \sum_{n=0}^{10} \mathbf{u}'_n(t) \Pi_n(z)$ —uses a least squares fit method (Alford 2003; Nash et al. 2005; Zhao et al. 2010).

Combining \mathbf{u}' , p' , and ξ (indices referring to modes are omitted in the following) allows computation of the depth-integrated baroclinic kinetic (KE) and potential energy (PE) densities,

$$\text{KE} = \left\langle \frac{1}{2} \int_{-H}^0 \rho(u'^2 + v'^2) dz \right\rangle (\text{J m}^{-2}), \quad \text{and} \quad (16)$$

$$\text{PE} = \left\langle \frac{1}{2} \int_{-H}^0 \rho(N^2 \xi^2) dz \right\rangle (\text{J m}^{-2}), \quad (17)$$

as well as the horizontal energy flux \mathbf{F} :

$$\mathbf{F} = \left\langle \int_{-H}^0 \mathbf{u}' p' dz \right\rangle (\text{W m}^{-1}). \quad (18)$$

In Eqs. (16)–(18), $\langle \cdot \rangle$ denotes an average over a wave period (M_2 here).

c. Barotropic tide energy loss using a tidal model

Following Egbert and Ray (2000), we compute the dissipation rate of the barotropic tide D as

$$D = W - \nabla \cdot \mathbf{P} (\text{W m}^{-2}), \quad (19)$$

where W is the work done by the barotropic tide, and \mathbf{P} is the barotropic tide energy flux. The flux \mathbf{P} is defined as

$$\mathbf{P} = \rho_0 g \langle \mathbf{U} \zeta \rangle, \quad (20)$$

where ζ is the tidal elevation, and \mathbf{U} is the barotropic tide volume transport, both extracted from TPXO. The work W is defined as

$$W = \rho_0 g \langle \mathbf{U} \cdot \nabla (\zeta_{\text{eq}} + \zeta_{\text{sal}}) \rangle, \quad (21)$$

where ζ_{eq} is the equilibrium tidal elevation, and ζ_{sal} is the tidal elevation induced by the tide's self-attraction and loading (Ray 1998).

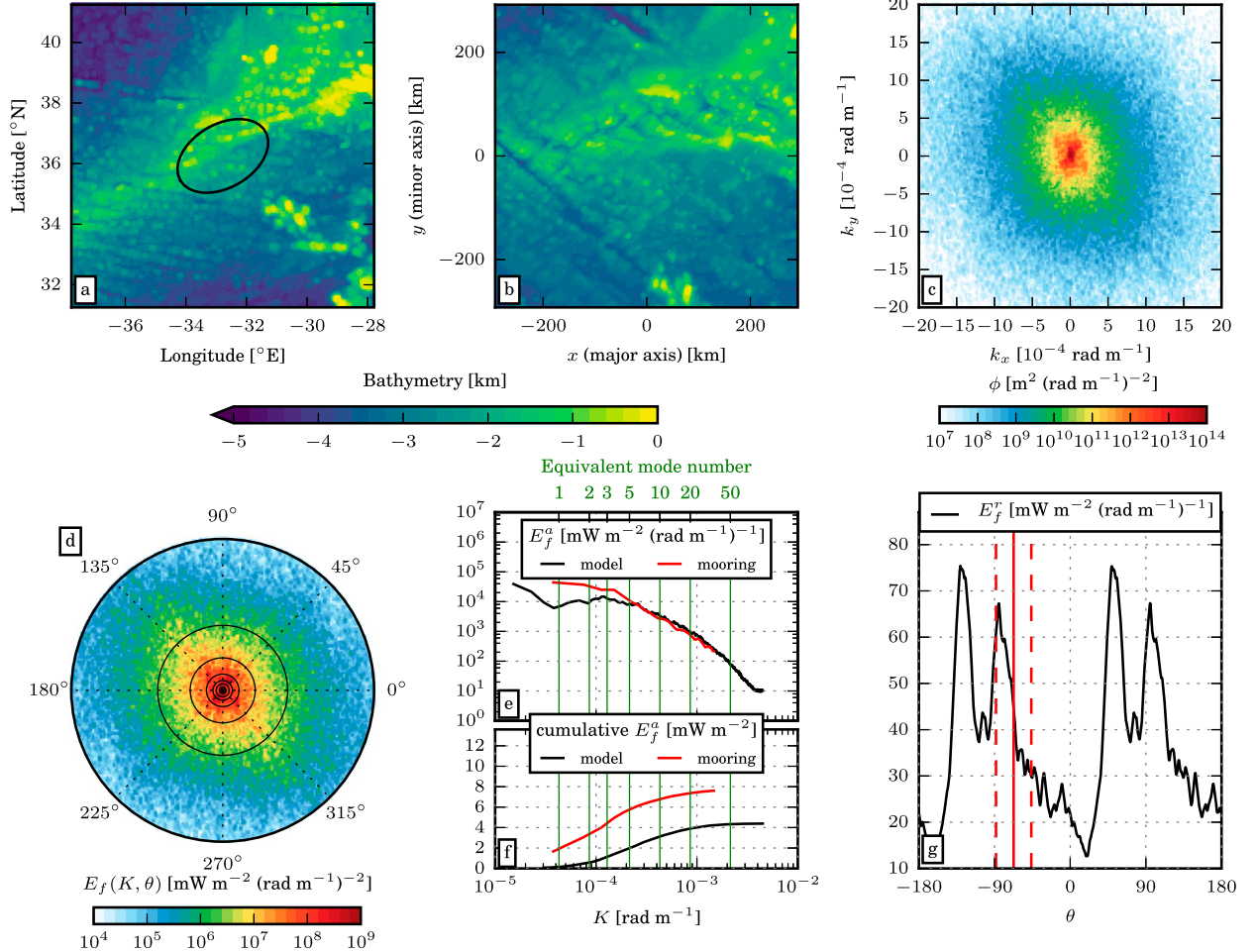


FIG. 3. Illustration of the method used in the barotropic-to-baroclinic energy conversion model at the mooring location. (a) Bathymetry in longitude–latitude coordinates and barotropic tidal ellipse. (b) Bathymetry in the rotated coordinate system aligned with the major x and minor y axes of the ellipse. (c) Two-dimensional power spectrum of bathymetry ϕ (k_x and k_y are the wavenumbers in the x and y directions, respectively). (d) Vertical energy flux $E_f(K, \theta)$ from Eq. (2); $\theta = 0$ in the x direction and rotates anticlockwise. (e) Azimuthally averaged vertical energy flux E_f^a from Eq. (3). (f) Cumulative E_f^a and (g) radially integrated vertical energy flux E_f^r from Eq. (4). Green lines in (e) and (f) are the equivalent mode numbers as labeled on top axis. Red plain and dashed lines in (g) are the mean direction of the mooring-derived energy flux and its standard deviation, respectively. Energy flux in (d)–(g) is computed for the M_2 frequency.

4. Structure of the semidiurnal internal tide

In this section, we use a range of measurements and a theoretical model to assess the life cycle of internal tides over the MAR at the location of the RidgeMix mooring—from generation (section 4a) to propagation (section 4b) and dissipation (section 4c)—before offering a summary of this local perspective (section 4d).

a. Theoretical estimates of internal tide generation

Figure 3 illustrates the method used to estimate barotropic-to-baroclinic energy conversion (section 3a) at the specific mooring location. First, the method interpolates the barotropic tidal ellipse from TPXO at the point of interest and extracts topography from

SRTM30_PLUS around it (Fig. 3a). Second, topography is rotated along the ellipse’s axes (Fig. 3b), and its two-dimensional power spectrum ϕ is computed (Fig. 3c). Third, ϕ is directionally weighted by tidal currents and multiplied by a factor depending on the three frequencies of the system (f , ω , and N_b) to give the vertical energy flux $E_f(K, \theta)$ [Eq. (2) and Fig. 3d]. Finally, E_f is azimuthally averaged to get its distribution as a function of horizontal wavenumber (Fig. 3e) or equivalently its modal distribution [Eq. (7)]. Its cumulative sum eventually gives the total energy conversion (Fig. 3f). Alternatively, E_f can be integrated in the wavenumber direction to get its azimuthal dependence (Fig. 3g).

The model predicts an energy conversion at the mooring site that spans a wide range of equivalent

horizontal wavenumbers, noticeably exhibiting a plateau between modes 1 and 5 and then gradually decreasing (Fig. 3e). Indeed, the rough topography of the MAR varies strongly on a wide range of scales, down to abyssal hill scales of $O(1)$ km (Goff 1991). As a consequence, high-mode internal tides are expected to be radiated, as observed (St. Laurent and Nash 2004) and modeled (Zilberman et al. 2009) on the flanks of the MAR in the Brazil Basin. Superimposed on the theoretical model estimates is the spectrum of mooring-derived horizontal energy flux, converted to a vertical flux by multiplying by α , the wave characteristic slope, and dividing by the water depth. The energy flux is cut at mode 35, which is in theory the highest mode that can be resolved with 36 independent thermistors.⁴ It shows a good agreement with the theoretical model for modes higher than 5 but overestimates energy fluxes in modes 1–4 (Fig. 3e). Nonetheless, we do not expect a perfect match, as the mooring detects fluxes from remote sources—most likely propagating low modes—that are not taken into account in the model. The total vertical energy flux is 4.5 mW m^{-2} in the model and 9.1 mW m^{-2} in the mooring data. A factor of 2 discrepancy is also found by St. Laurent and Nash (2004). This may also relate to the model's failure to take account of the subtidal circulation, which could introduce variability in internal tide generation (Kerry et al. 2014).

The model predicts the direction of the flux modulo 180° (Fig. 3g). The two preferential directions are almost perpendicular to the tidal ellipse's major axis ($\theta = 0$) and coincides roughly with the cross-fracture zone direction (Fig. 3a). The mooring-derived flux is mainly to the southeast and roughly fits in the prediction of the model (Fig. 3g). Again, we do not expect a perfect match since the model is local and cannot take into account remote modulation of the flux.

b. Internal tide properties from high-resolution mooring data

1) ENERGY DENSITY AND ENERGY FLUX

Time series of energy density $E = \text{KE} + \text{PE}$ and horizontal energy flux $F = ||\mathbf{F}||$ in modes 1–10 are shown in Figs. 4d and 4e. The energy density is mostly contained in mode 1 and gradually decreases with increasing mode number (Fig. 4d). The horizontal energy flux is, on the other hand, overwhelmed by mode 1,

which is almost indistinguishable from the total energy flux (Fig. 4e). This picture is consistent with open-ocean mooring estimates of energy density and energy fluxes from the Internal Waves Across the Pacific experiment (IWAP; Zhao et al. 2010). Indeed, on the one hand, the wave velocity \mathbf{u}' and displacement ξ' project qualitatively onto a few modes, between 1 and 10 (not shown). On the other hand, the wave pressure p' results from the vertical integration of ξ' and is hence smoother and thus is dominated by low modes. As a consequence, the kinetic [Eq. (16); Fig. 4b] and potential energy [Eq. (17); Fig. 4c] computed from \mathbf{u}' and ξ' have some contributions from modes 1–10. In contrast, the horizontal energy flux [Eq. (18); Fig. 4e] computed from \mathbf{u}' and p' is strongly dominated by mode 1. The time-mean and standard deviation of E and F as a function of mode confirm this distribution (Figs. 5a,b; Table 1). The mode-1 energy flux accounts for 83% of the energy flux of modes 1–10. However, mode-1 energy density accounts for only 45% of the energy density of modes 1–10. Our basic interpretation is that although the bulk of—potentially—propagating energy is in mode 1, mode 2 and above (modes higher than 10 are partially captured by the mooring) contain at least 55% of the energy ultimately available for local mixing.

The robustness and steadiness of mode-1 flux compared to higher modes is also demonstrated by the time series of their direction (Fig. 4f). The mode-1 flux is always directed between east and south directions and varies slowly, likely influenced by the surrounding mesoscale eddy field (Rainville and Pinkel 2006; Dunphy et al. 2017). On the other hand, the mode-2 and mode-3 flux directions vary through all azimuths on daily time scales. A similar variability is found for modes greater than 3 (not shown). This short time-scale variability might be attributed to interferences between waves arising from different sources, reflection, and scattering (e.g., Zaron and Egbert 2014). Two-dimensional histograms of modal horizontal energy fluxes further confirm the multidirectional nature of fluxes for modes greater than 1 (Fig. 6). This high directional variability is probably linked to the multiple sources of internal tides on the MAR around the mooring. The recent comparison of mode-1 and mode-2 horizontal energy fluxes from a high-resolution numerical model and historical moorings further demonstrates a poorer correlation and a higher variability in mode-2 fluxes compared to mode-1 fluxes (Ansorg et al. 2017).

2) GROUP VELOCITY

Following the method of Alford et al. (2006) and Alford and Zhao (2007b), we compute the group

⁴This assumes that the spacing between thermistors is perfectly designed to capture the vertical structure of high modes (Fig. 2), which may not be the case for the highest modes.

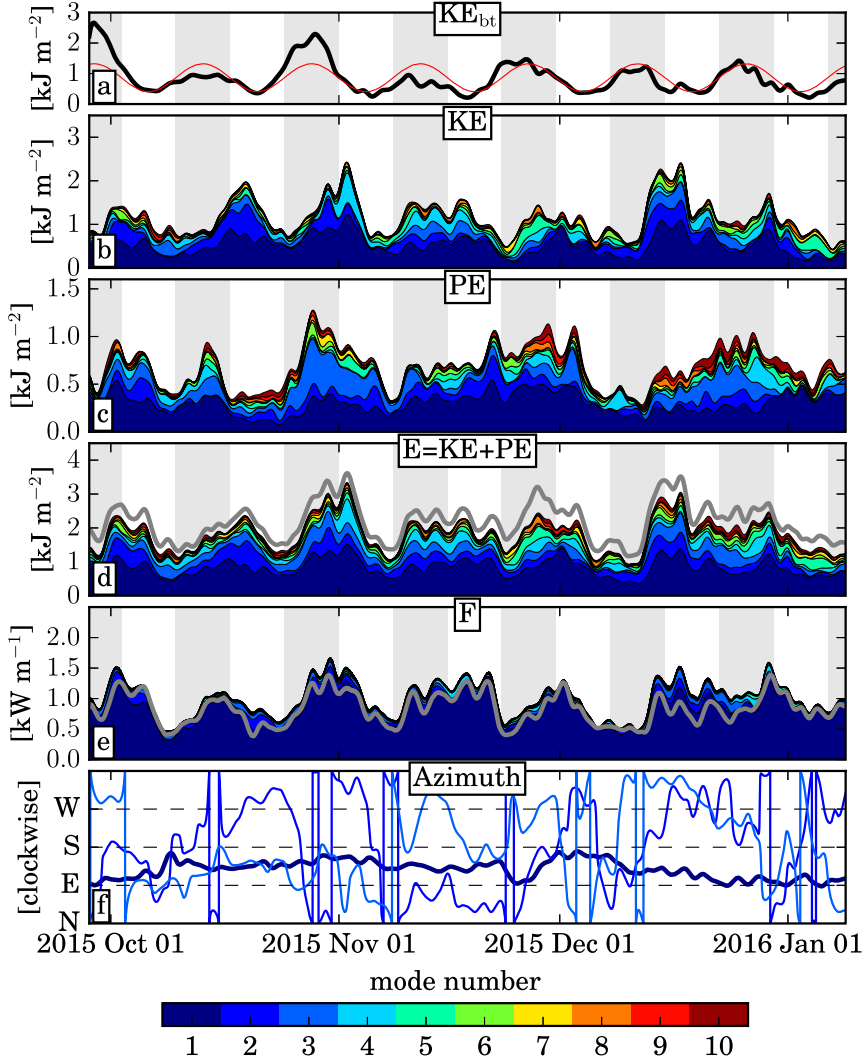


FIG. 4. Time series of (a) barotropic kinetic energy KE_{bt} estimated from the moored ADCPs (black line) and from the TPXO combination of M_2 and S_2 tidal velocities (red line). Cumulated variables as a function of mode number: (b) KE , (c) PE , (d) $E = KE + PE$, (e) horizontal energy flux F , and (f) azimuth of mode-1 (thick line), mode-2, and mode-3 fluxes (colors follow the color bar). Gray lines in (d) and (e) are total E and F , respectively; no modal decomposition is performed. Gray shading in (a)–(e) represents spring tides. Notice that the flux from the total field can be smaller than the sum of the modal contributions as fluxes in different modes are not necessarily oriented in the same directions.

velocity of each mode from mooring estimates of energy density and horizontal energy flux $c_g^m = F/E$. The method exploits the strong correlation between E and F (scatterplots in Figs. 7a,c). Briefly, the mean energy and standard deviation are first estimated in each energy flux bin (we chose 10 evenly spaced bins between extreme flux values). The slope, that is, c_g^m , and its 95% confidence interval are then computed by linear regression. Probability density functions (PDFs) of the populations of F/E also give an overview of the distribution (Figs. 7b,d). Estimates of c_g^m are compared to

theoretical values of group velocity for freely propagating waves:

$$c_g = c_n \frac{(\omega^2 - f^2)^{1/2}}{\omega}, \quad (22)$$

where c_n is the mode- n eigenspeed [Eq. (14)]. Alford and Zhao (2007b) also developed a simple model for the perceived group velocity of a standing wave resulting from the interaction of two waves propagating in the opposite direction (see also Nash et al. 2004).

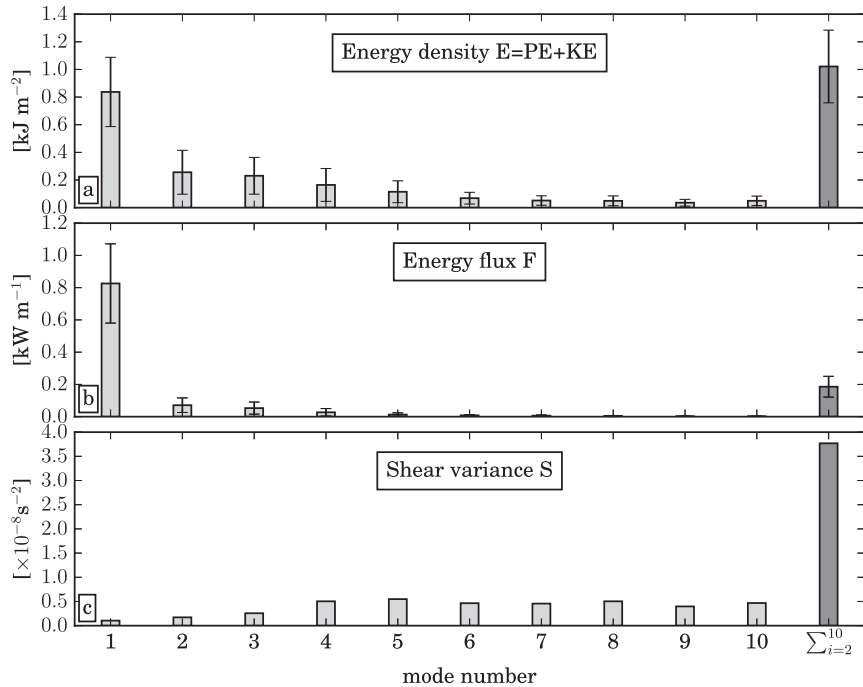


FIG. 5. Time-mean (a) energy density E , (b) horizontal energy flux F , and (c) shear variance S in modes 1–10 (light gray bars) and in the sum of modes 2–10 (dark gray bars). Error bars are standard deviations from the mean.

This perceived group speed c_g^s is a spatial modulation of c_g :

$$c_g^s = \frac{2\omega f \sin(2kx)}{\omega^2 - f^2 \cos(2kx)} c_g, \quad (23)$$

where k is the wavenumber in the x direction (see appendix in Alford and Zhao 2007b). In the following, c_g^s refers to the mean group velocity over one wavelength.

The estimated mode-1 group velocity ($1.09 \pm 0.10 \text{ m s}^{-1}$) agrees particularly well with the group velocity of a standing wave (1.08 m s^{-1} ; Fig. 7a and Table 1). Interestingly, the peaks of the bimodal-like shape of the PDF of F/E coincide with c_g and c_g^s (Fig. 7b). This suggests that although the mode-1 wave is most of the time consistent with a standing wave, specific events are more compatible with a propagating wave.

The mode-2 group velocity shows a different picture, being inconsistent with both propagating and standing wave velocities (Fig. 7c). Estimates of c_g^m are smaller than c_g and c_g^s by 48% and 37%, respectively. Such discrepancies in mode-2 group velocities with theoretical estimates are also reported over the MAR in Alford and Zhao (2007b). They attribute this slow apparent propagation to the multidirectional fluxes—observed for modes greater than or equal to 2 here (Figs. 6b–f)—that decohere the waves.

We applied the same technique to modes 1–10 and report the estimated group velocity with their 95% confidence interval in Fig. 8. Apart from mode 4, which is more consistent with a propagating wave, all modes are either more compatible with standing waves or have even smaller group velocities than expected from a standing wave. Modes greater than 8 have very small

TABLE 1. Energy density E (kJ m^{-2}), horizontal energy flux F (kW m^{-1}), estimated group velocity c_g^m (m s^{-1}), and theoretical group velocity (m s^{-1}) for propagating c_g and standing c_g^s waves in modes 1–10. Errors are standard deviations for E and F and 95% confidence interval for c_g^m .

Mode	1	2	3	4	5	6	7	8	9	10
E	0.84 ± 0.25	0.26 ± 0.16	0.23 ± 0.13	0.16 ± 0.12	0.11 ± 0.08	0.07 ± 0.04	0.05 ± 0.03	0.05 ± 0.04	0.04 ± 0.02	0.05 ± 0.03
F	0.83 ± 0.25	0.07 ± 0.05	0.05 ± 0.04	0.03 ± 0.02	0.01 ± 0.01	0.01 ± 0.01	0.01 ± 0.00	—	—	—
c_g^m	1.09 ± 0.10	0.34 ± 0.05	0.33 ± 0.04	0.33 ± 0.03	0.23 ± 0.03	0.19 ± 0.03	0.16 ± 0.01	0.11 ± 0.01	0.06 ± 0.02	0.05 ± 0.01
c_g	1.33	0.66	0.44	0.33	0.27	0.22	0.19	0.17	0.15	0.13
c_g^s	1.08	0.54	0.36	0.27	0.22	0.18	0.15	0.14	0.12	0.11

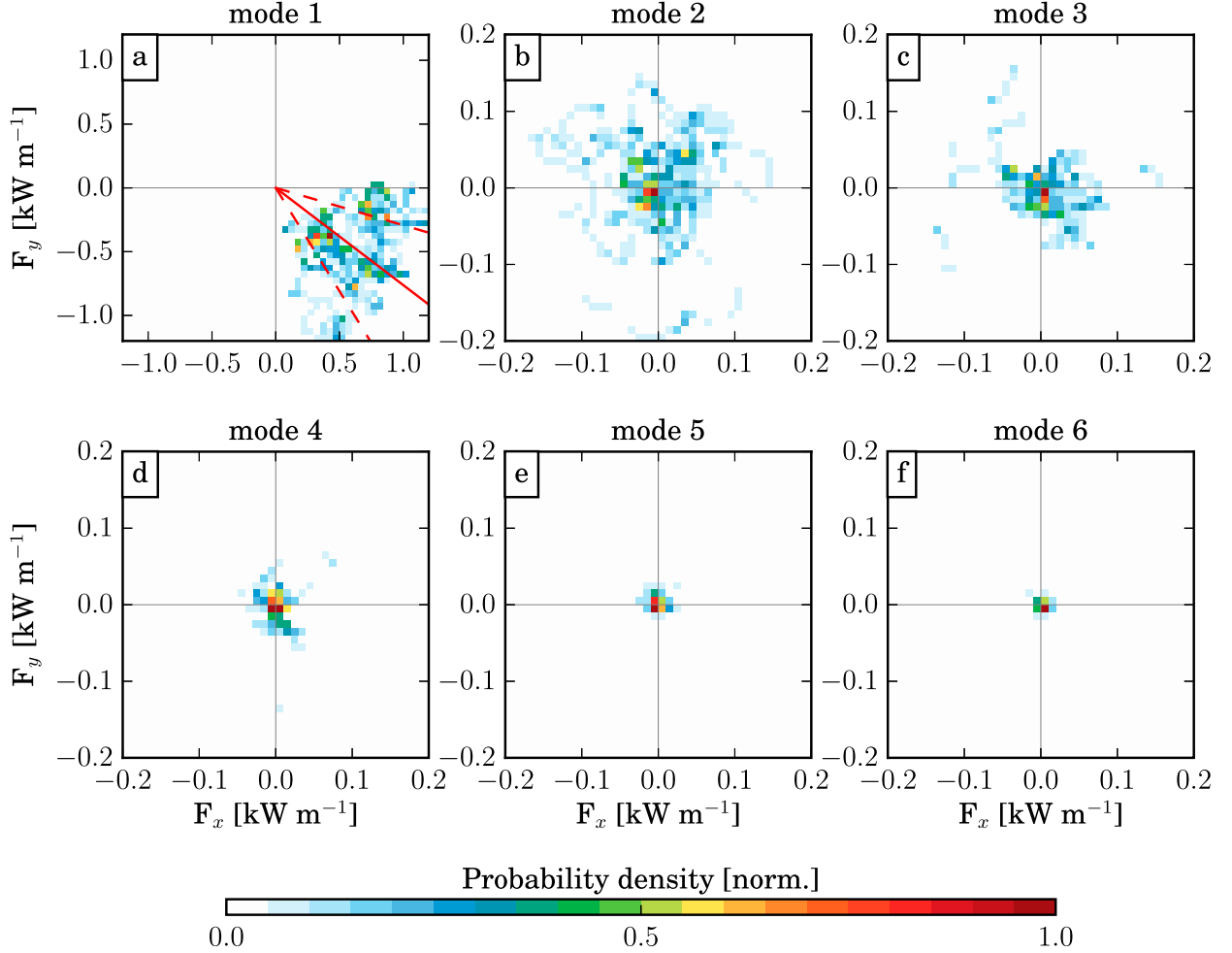


FIG. 6. Normalized histogram of horizontal energy flux for (a)–(f) modes 1–6. The ranges of x and y axis differ between (a) and (b)–(f). Red solid and dashed lines in (a) represent the mean flux direction (azimuth 127.3°) and standard deviation (21.0°), respectively.

group velocity because of vanishing fluxes, and their velocities thus gradually depart from theoretical values.

3) SPRING–NEAP CYCLE

The energy density and horizontal energy flux both display a remarkable spring–neap cycle, mostly dominated by mode 1 (Figs. 4d,e). This spring–neap cycle is obviously related to the astronomical forcing, as seen in barotropic kinetic energy $\text{KE}_{\text{bt}} = \int_{-H}^0 (1/2)\rho \|\mathbf{u}\|^2 dz$ (Fig. 4a). Time series of KE_{bt} from the mooring shows a good agreement with a synthetic estimate from the combination of M_2 and S_2 computed from TPXO (red line in Fig. 4a). Major peaks at the end of September and October might be associated with other long-term astronomical forcing frequencies that amplify the semidiurnal signal.

The time lag between KE_{bt} and E is estimated in lag-correlating time series, previously bandpassed filtered at

the spring–neap cycle (Alford and Zhao 2007a). The maximum correlation is 0.69 and is reached for a 3.4-day lag. We conjecture that the spring–neap variability—mostly seen in mode 1—is triggered by remotely generated mode-1 internal tides that propagate up to the mooring site. To track down the origin of these waves, we make use of the Zhao et al. (2016) dataset, which decomposes the internal tide properties (SSH and horizontal energy fluxes) into their northbound and southbound components (Figs. 9a,b). Notice that this dataset contains only M_2 internal tides, whereas the mooring analysis contains all semidiurnal constituents. However, we checked that the M_2 surface tide kinetic energy dominates over other semidiurnal constituents by an order of magnitude regionally (not shown), so we expect M_2 to also dominate the internal wave field. The Zhao et al. (2016) dataset reveals that the Atlantis-Meteor Seamount Complex [green contours in Figs. 9a,b; see also Fig. 1 in

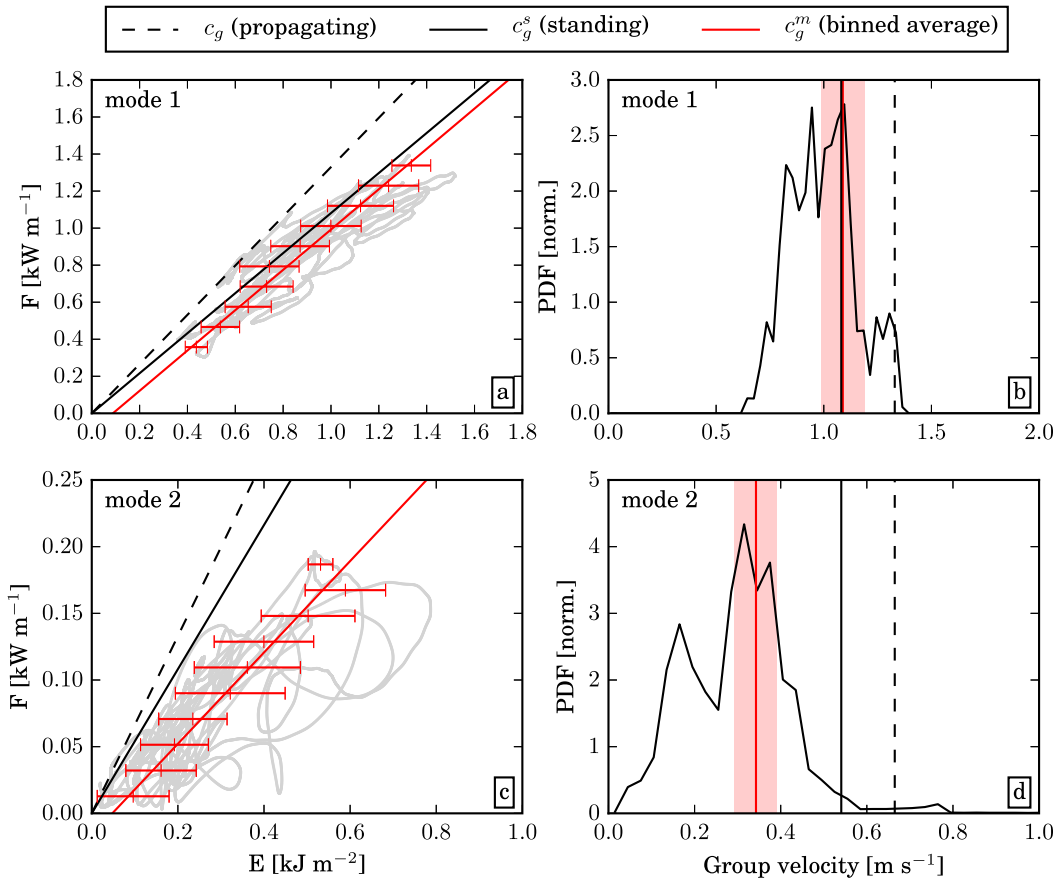


FIG. 7. Figure inspired by Fig. 1 in Alford and Zhao (2007b). (a),(c) Scatterplot of semidiurnal horizontal energy flux vs energy density (gray dots), mean and standard deviation of energy in each energy flux bin (red bars), and linear regression to these points (red lines) for mode-1 in (a) and mode-2 in (c). Group velocity is determined by the slope of this linear regression. The dashed and solid lines represent theoretical group velocity for propagating c_g and standing c_g^s waves, respectively. (b),(d) Probability density function of each population of $c_g^m = F/E$ for mode-1 in (b) and mode-2 in (d). The binned average group velocity and its 95% confidence interval are shown in red. The quantities c_g and c_g^s are also shown in solid and dashed lines, respectively.

Searle (1987) for a wider geographical setting] is a regional hot spot for mode-1 internal tide generation. In particular, a northbound beam emanates from the Hyères Seamount (31.3°N , 28.9°W ; green star in Fig. 9a) and points toward the mooring site, following the orange line in Fig. 9a. SSH interpolated along this line shows a clear oscillating signal with a decreasing amplitude along the path (Fig. 9c). The traveling time $t(x)$, as a function of distance from the source x , for this semidiurnal mode-1 internal tide is estimated as

$$t(x) = \int_{x_s}^x \frac{x'}{c_g(x')} dx', \quad (24)$$

where x_s is the seamount coordinate, and c_g is the mode-1 group velocity defined in Eq. (22). Figure 9d shows the spatial variability of c_g —mostly depending on the

bathymetry (Fig. 9c)—and the traveling time throughout the propagation. In theory, the internal tide reaches the mooring site in ~ 4 days, which is comparable to the 3.4-day lag between the astronomical forcing and the oceanic response. As such, the internal tide generated at the Hyères Seamount is a good candidate to explain the spring–neap modulation of energy density and horizontal energy flux measured at the mooring site. Notice that its energy flux is roughly in the opposite direction to the flux diagnosed at the mooring site. Hence, the superposition of the two waves is coherent with the diagnosed standing group velocity at the mooring site.

c. Local dissipation from microstructure measurements

Two 25-h stations with continuous tethered VMP deployments were carried out in the vicinity of the

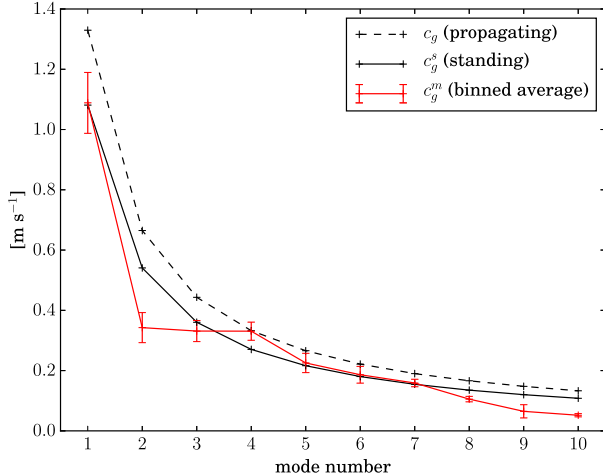


FIG. 8. Binned average group velocity and its 95% confidence interval for modes 1–10, as determined as in Fig. 7 (red line). Theoretical group speeds for propagating c_g and standing c_g^s waves are shown in dashed and solid black lines, respectively.

mooring site during spring and neap tides (section 2a). Mean profiles of the turbulent dissipation rate ε and the PDF of $\log(\varepsilon)$ for both series of casts are shown in Fig. 10. There is evidence for intensified dissipation during the spring tide, as highlighted by the spring tide PDF of $\log(\varepsilon)$ being skewed toward higher values compared to the neap tide PDF (Fig. 10b). Vertical profiles of ε also reveal a higher springtime dissipation at almost all depths with enhanced differences in the bottommost 500 m (Fig. 10a). In this depth range, ε reaches $10^{-9} \text{ W kg}^{-1}$, as routinely observed over rough topography of the world's oceans (Kunze 2017). Notice that the tethered VMP could not dive deeper than $\sim 400 \text{ m}$ above the seafloor ($\sim 2200 \text{ m}$) because of wire length limitations, and we expect dissipation to further increase with depth in excess of 1800 m.

The depth-integrated dissipation ε_z [Eq. (1)] is $1.3 \pm 1.1 \text{ mW m}^{-2}$ during spring tide and $0.7 \pm 0.4 \text{ mW m}^{-2}$ during neap tide. A similar factor of 2 difference between spring and neap tide dissipation has been observed on the Hawaiian Ridge (Klymak et al. 2006). Notice that ε_z is likely to be underestimated because of undersampling of the water column. Nonetheless, these high levels of dissipation may be due to the enhanced local generation of high-mode internal tides that carry most of the shear variance (Fig. 5c) and are prone to rapid breaking close to their generation site (in a similar fashion as on the Oregon continental slope; Nash et al. 2007). In addition, the spring–neap modulation and bottom intensification of dissipation suggests that the elevated turbulence may be triggered by a direct breaking of high-mode internal tides (Klymak et al. 2008). Note, however, that we are unable to verify that

the spring–neap component of dissipation is phase locked with astronomical forcing.

d. Summary of the local perspective

In summary, the high-resolution mooring data provide us with a detailed insight into internal tide dynamics on the northern MAR. The horizontal energy flux is highly dominated by mode 1 (0.83 kW m^{-1}) and is rather steady in direction. Its intensity displays a strong spring–neap cycle lagging by 3.4 days from the astronomical forcing, hence pointing to a modulation by remote sources. The Hyères Seamount—a hot spot of mode-1 internal tide generation of the Atlantis-Meteor Seamount Complex—is a very likely candidate as it radiates an internal tide beam toward the mooring site, whose traveling time is close to the spring–neap cycle lag to the astronomical forcing.

The horizontal energy fluxes associated with modes 2–10 are very weak ($< 0.07 \text{ kW m}^{-1}$) and vary strongly in direction, likely caused by the interactions of waves generated by numerous, distributed sources on the MAR. In turn, the energy density is more widely partitioned between modes, with mode 1 accounting for a smaller fraction of the total energy density than the sum of modes 2–10 (0.84 vs 0.95 kJ m^{-2}). Examination of the propagation velocity revealed that most of the modes are compatible with standing waves. This implies that internal tide energy is likely to remain concentrated over the MAR and thereby become ultimately available for near-local turbulent mixing. In line with this result, microstructure measurements performed at the mooring site reveal elevated and bottom-intensified turbulent energy dissipation. The energy conversion model further confirms that high modes are expected to be generated. The model possibly underestimates conversion into low modes—although low modes diagnosed from mooring data may originate from remote sources (Figs. 9a,b)—but its agreement with mooring-derived fluxes for modes greater than 3 is remarkable.

5. Regional perspective

To get a broader view of internal tide dynamics over the northern MAR, we performed a regional energy budget using different data sources. The barotropic tide energy loss and internal dissipation should be equal in the absence of energy transport by internal tides. However, low-mode internal tides play a role in redistributing energy. In addition, energy entering low modes does not dissipate locally. In the following, the barotropic tide energy loss D is estimated via a tidal model (section 3c), the tidal barotropic-to-baroclinic conversion E_f is estimated via a two-dimensional spectral

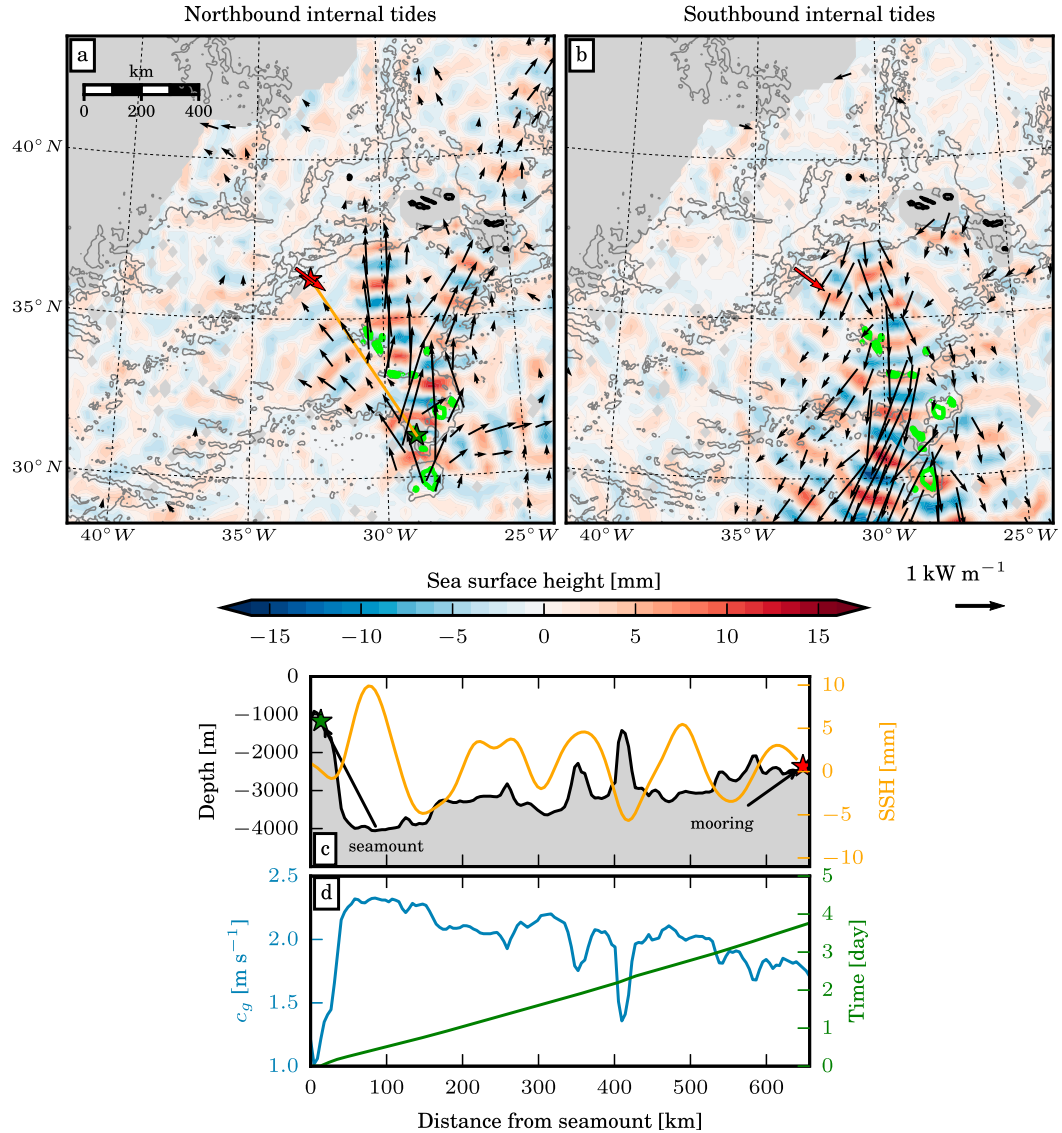


FIG. 9. (a) Northbound and (b) southbound M_2 mode-1 internal tides from the [Zhao et al. \(2016\)](#) dataset; color is SSH, and arrows are horizontal energy fluxes (fluxes smaller than 0.2 kW m^{-1} have been masked). The masked region in gray in the northwest corner is where mesoscale activity is too strong to be properly separated from internal tides (overlap in scales). The red arrow is the time-mean mode-1 horizontal energy flux from the mooring data. Black lines are the 2000- and 4000-m bathymetry contours. Green lines southward of 35°N are the 1000-m bathymetry contours highlighting the Atlantis-Meteor Seamount Complex, a chain of seamounts extending from the Great Meteor Seamount at its southern edge to the Atlantis Seamount at its northern edge (see also Fig. 1 in [Searle 1987](#)). Red and green stars are locations of the mooring and the Hyères Seamount, respectively. (c) Bathymetry (black line) and SSH (orange line) interpolated along the orange line in (a), stretching from the Hyères Seamount to the mooring location. (d) Theoretical group speed (light blue) and traveling time (green) of a M_2 mode-1 internal tide propagating along the orange line in (a).

model (section 3a), and the conversion to mode-1 internal tide is also estimated via satellite altimetry $(\nabla \cdot \mathbf{F}_s^l)^+$ (section 2b and [Zhao et al. 2016](#)). For this exercise, we extended the conversion model to a regional domain spanning from 22°N (southern edge of the RidgeMix cruise) to 42°N , slightly north of the Azores.

Using global datasets described in section 2b, we computed E_f on a regular $1/4^\circ$ grid.

The regional distribution of the total energy conversion E_f^t , the mode-1 energy conversion E_f^1 , the energy conversion into modes $\geq 2 E_f^{2-\infty}$, the barotropic tide energy loss D , and the satellite estimate of mode-1

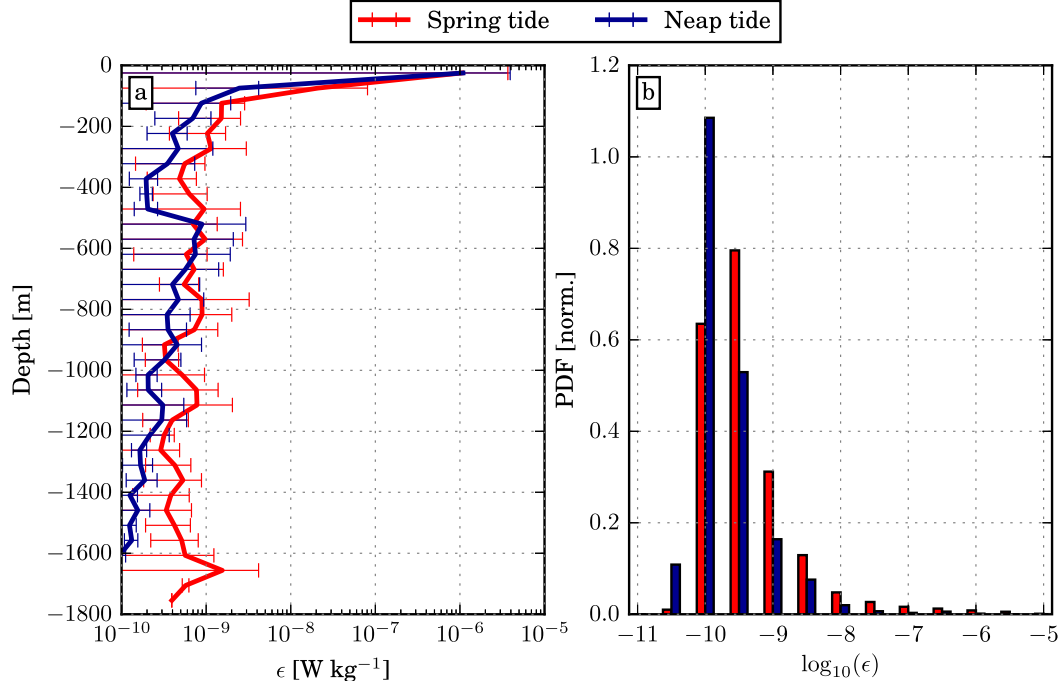


FIG. 10. (a) Vertical profile of 50-dBar binned dissipation ϵ (mean and std dev) and (b) PDF of $\log(\epsilon)$ from repeated tethered VMP casts in the close vicinity of the mooring site during spring tide (red) and neap tide (blue).

energy conversion ($\nabla \cdot \mathbf{F}_s^1$)⁺ are shown in Figs. 11a–e. The highest levels of conversion ($>10\text{ mW m}^{-2}$) are mostly found at depths shallower than 2000 m near the Azores and the Atlantis-Meteor Seamount Complex. This is due to strong barotropic currents and increased bottom stratification associated with shallower depths. The regions of strong barotropic tide energy loss are collocated with these areas, although they are more spatially widespread around the Atlantis-Meteor Seamount Complex. Other hot spots of conversion ($>5\text{ mW m}^{-2}$) are found on the edge of the MAR. This is where topography is roughest, thus contributing to a rich energy conversion through a broad range of scales as highlighted in section 4.

The energy conversion into mode 1 agrees well between the two independent estimates (Figs. 11b,e). As shown above, the Atlantis-Meteor Seamount Complex is the main source of mode-1 internal tides (see Figs. 9a,b). Another hot spot is the Azores Islands, which the satellite product misses likely because of the proximity of land. Importantly, both products concur on a very low mode-1 conversion at the MAR ($<1\text{ mW m}^{-2}$). In contrast, strong generation of modes ≥ 2 occurs on the MAR and accounts for most of the energy conversion (cf. Figs. 11a and 11c). Using a different method for estimating energy conversion into normal modes, Falahat et al. (2014b) demonstrate a qualitatively similar distribution (their Fig. 6).

All quantities are further summed over the hatch-free area in Figs. 11a–e, where the ocean depth lies between 200 and 4000 m. This area isolates the MAR and does not include the Azores Plateau, where the assumption of small tidal excursion is likely to be violated. Two robust conclusions can be drawn from this budget (Fig. 11f). First, the close agreement between D (16.4 GW) and E_f^t (13.7 GW) confirms previous assumptions that most of the energy dissipated by the barotropic tide in the deep ocean is converted into internal tides—84% here—and not dissipated by bottom friction like on continental shelves (e.g., Egbert and Ray 2000). Second, more specific to the northern MAR, energy conversion into mode 1 only accounts for 9% (1.2 GW) of the total conversion (7% of the barotropic tide energy loss), and higher modes thus represent the bulk of the energy conversion (12.4 GW; 81%). The satellite product confirms the modest contribution of mode 1 (1.7 GW).

As a point of comparison, the Hawaiian Ridge system dissipates 20 GW of barotropic tidal energy (Egbert and Ray 2001), of which 6 GW (30%) is converted into mode 1 (Merrifield and Holloway 2002). The difference between the distribution of energy stems from the different topographic shapes of the two ridge systems. The Hawaiian Ridge has abrupt flanks that generate intense mode-1 tides, which may propagate far away from the ridge (Zhao et al. 2010). In contrast, the MAR has a

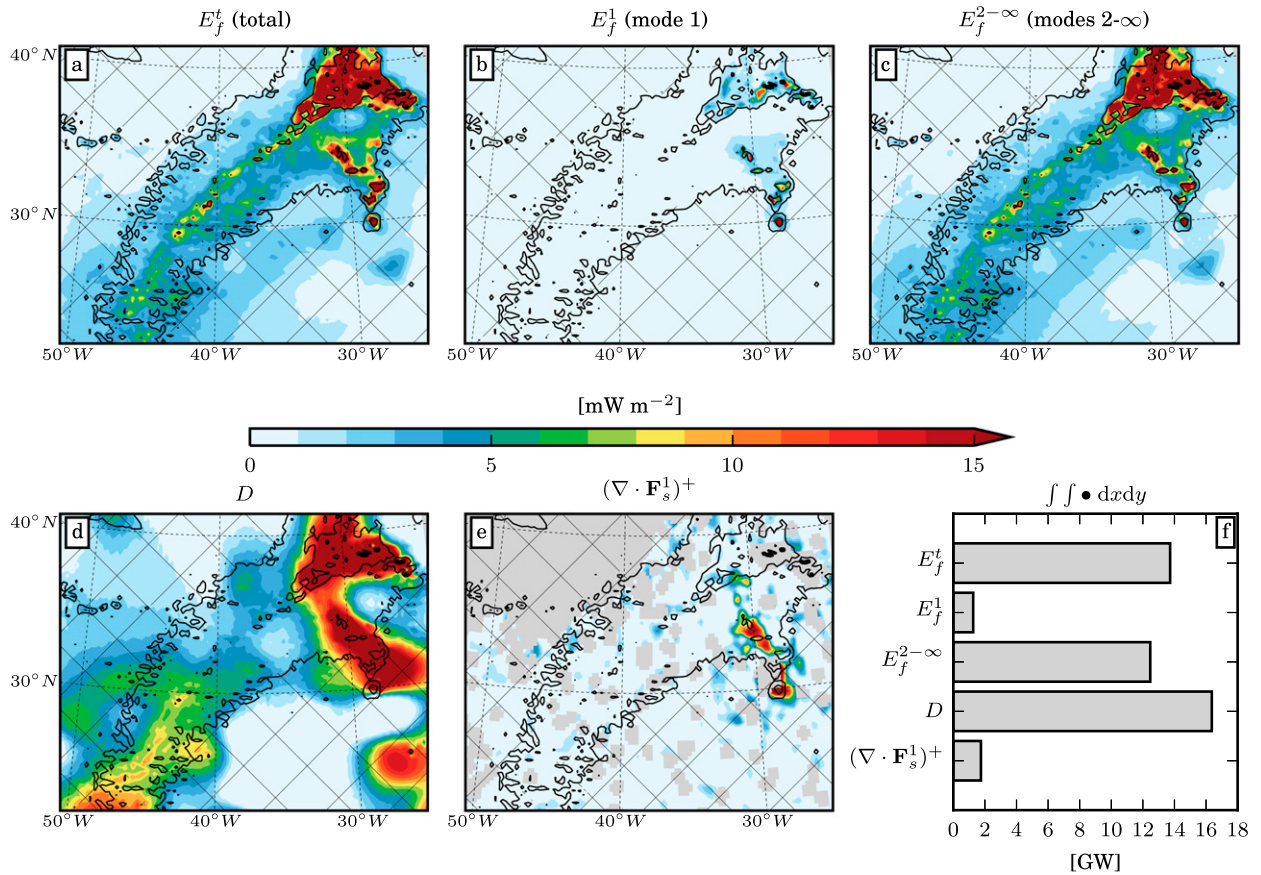


FIG. 11. Model estimate of barotropic-to-baroclinic energy conversion: (a) E_f^t from Eq. (5) and (b) E_f^1 and (c) $E_f^{2-\infty}$ from Eq. (6). (d) Energy loss from the barotropic tide D from Eq. (19). (e) Energy conversion into mode 1 estimated from satellite altimetry $(\nabla \cdot \mathbf{F}_s^1)^+$ (Zhao et al. 2016). (f) Area-integrated quantities $\iint \{E_f^t, E_f^1, E_f^{2-\infty}, D, (\nabla \cdot \mathbf{F}_s^1)^+\} dx dy$ over the hatch-free region shown in (a)–(e). Corrugated black lines in (a)–(e) are the 2000- and 4000-m bathymetry contours. The masked region in gray in the northwest corner of (e) is where mesoscale activity is too strong to be properly separated from internal tides (overlap in scales).

wider rift valley (in the fracture zone direction, the direction perpendicular to the ridge edge) and hosts taller and steeper abyssal hills because of its slow spreading rate (Goff 1991). The latter are known to generate high-mode internal tides (Melet et al. 2013; Lefauve et al. 2015; Timko et al. 2017) that are prone to rapid breaking.

The VMP data allow us to gain some insight into the distribution in turbulent dissipation levels across and beyond the MAR (Fig. 12). The most notable feature is the strong on- versus off-ridge contrast, with increased dissipation occurring above the rough topography of the MAR [as also evidenced in the Brazil Basin by Polzin et al. (1997) and Ledwell et al. (2000)]. Pointwise dissipation rate is often $\geq 10^{-9} \text{ W kg}^{-1}$ over the ridge and decays to $O(10^{-11}-10^{-10}) \text{ W kg}^{-1}$ off the ridge (Fig. 12b). The vertical distribution of ε is beyond the scope of this study, and we focus on the depth-integrated dissipation ε_z from 50 m (to exclude

turbulence related to mixed layer processes) to the seafloor [Eq. (1); Fig. 12a]. The dissipation ε_z and the local energy conversion E_f^t exhibit similar patterns, attaining maximum values on the ridge and minimum rates off the ridge. Note that ε_z is smaller than E_f^t everywhere, which is expected since a fraction of energy may radiate away.

The fraction of the local dissipation to the total energy conversion $q = \varepsilon_z/E_f^t$ enters current parameterizations (i.e., St. Laurent et al. 2002) for diapycnal mixing—tightly coupled to internal wave breaking—in general circulation models. Its value is often assumed constant and set to 0.3, although there is compelling evidence for strong geographical heterogeneity [q has been reported to vary from 0.05 to 0.60; see the review in MacKinnon et al. (2017)]. As the ocean stratification and global overturning circulation are highly sensitive to diapycnal mixing (Mashayek et al. 2015; de Lavergne et al. 2016), understanding the physics underpinning the regional

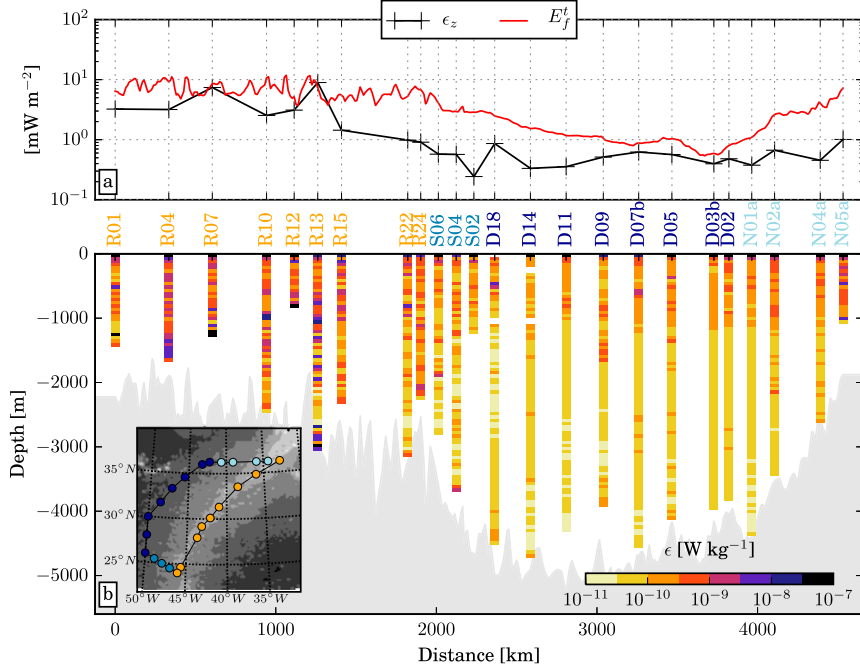


FIG. 12. (a) Depth-integrated dissipation ϵ_z (black line) and barotropic-to-baroclinic energy conversion E_f^t (red line) interpolated on the cruise track. (b) Section of 50-dBar binned dissipation from free-falling VMP stations represented by dots on the inset map and labeled on the top axis. The first station is at the northeastermost point (R01), and the section follows a clockwise rotation from R01. Bottom axis shows distance from R01 following the cruise track.

variability in q is important (MacKinnon et al. 2017). Here, a regional estimate of q on the northern MAR is 0.49 ± 0.35 (mean and std dev) for the nine stations on the ridge (yellow dots in Fig. 12, inset map). Notice that this estimate applies to the top of the MAR and takes into account E_f^t computed on a $1/4^\circ$ grid; thus, it is tight to a length scale of roughly 25 km. Our regional q is considerably higher than the 8%–25% estimated in Hawaii (Klymak et al. 2006), consistent with an enhanced generation of high-mode internal tides on the MAR. However, this estimate of q must be interpreted cautiously because of the relatively modest number of dissipation measurements and their poorly constrained representativeness, namely, linked to the spring–neap variability of dissipation (section 4c). Additional measurements with a greater spatiotemporal coverage would be needed to refine this estimate.

6. Conclusions

A multisource analysis of the life cycle of semidiurnal internal tides on the MAR sector south of the Azores has been conducted. The main conclusions are as follows:

- 1) Mooring data on top of the MAR reveal that the internal tide horizontal energy flux is dominated by mode 1, which is steady in intensity and direction (to the southeast). The mode-1 horizontal energy flux undergoes a strong spring–neap cycle that likely stems from interaction with remotely generated internal tides. Energy fluxes for modes greater than 1 are extremely variable in intensity and direction, probably because of interactions with ubiquitous, distributed sources on the MAR.
- 2) Energy density is more widely distributed among the modes. Specifically, modes 2–10 contain more energy than mode 1 alone. High-mode generation is supported by spectral estimates of energy conversion.
- 3) Estimates of modal group velocity indicate that most modes are compatible with standing internal waves. Given conclusion 2, this implies that energy is concentrated above the MAR and ultimately dissipates locally. This is supported by the strong energy dissipation inferred from microstructure measurements.
- 4) A simplified regional energy budget outlines qualitative differences with the well-studied Hawaiian

Ridge system (Merrifield and Holloway 2002; Klymak et al. 2006), which dissipates a similar amount of semidiurnal barotropic tide energy (16 GW over the MAR versus 20 GW around Hawaii). Namely, only 9% (vs 30% in Hawaii) of the energy is converted into mode 1, the only mode that may radiate energy away. Consistently, the fraction of energy locally dissipated is higher over the MAR, $q = 0.49 \pm 0.35$ versus 0.08–0.25 in Hawaii (Klymak et al. 2006). This measure is, however, rather uncertain given the modest number of direct dissipation measurements. Note that these results are in line with differences in internal tide characteristics between the two systems highlighted in St. Laurent and Nash (2004). Falahat et al. (2014a) also found a higher q in the Atlantic Ocean than in the Pacific Ocean. They attribute this difference to the extended sharp topography of the MAR as compared to the knife edge shapes of the Hawaiian Ridge and isolated seamounts in the Pacific Ocean.

A final perspective of this work is provided by the regional validation of the spectral estimate of energy conversion, which can be extended globally. This model is, by construction, more accurate than parameterizations (e.g., Nycander 2005; Green and Nycander 2013; and references therein) and gives additional information on the modal content and direction of the internal tide energy flux.

Acknowledgments. RidgeMix is supported by the U.K. Natural Environment Research Council through Grant NE/L004216/1. We are grateful to the technicians, officers, and crew of RRS *James Clark Ross* for their invaluable role in data collection. ACNG further acknowledges the support of the Royal Society and the Wolfson Foundation. ZZ was supported by NASA Ocean Surface Topography Science Team (OSTST) Award NNX17AH57G. The regional computation of energy conversion uses Python's mpi4py message passing interface library (Dalcin et al. 2008, 2011; <https://mpi4py.scipy.org/docs/mpi4py.pdf>). The code is available on request. Discussions with Christian Buckingham and Rob Hall are greatly appreciated. We appreciate the criticism of two reviewers that helped to improve the quality of the manuscript.

REFERENCES

- Alford, M. H., 2003: Redistribution of energy available for ocean mixing by long-range propagation of internal waves. *Nature*, **423**, 159–162, <https://doi.org/10.1038/nature01628>.
- , and Z. Zhao, 2007a: Global patterns of low-mode internal-wave propagation. Part I: Energy and energy flux. *J. Phys. Oceanogr.*, **37**, 1829–1848, <https://doi.org/10.1175/JPO3085.1>.
- , and —, 2007b: Global patterns of low-mode internal-wave propagation. Part II: Group velocity. *J. Phys. Oceanogr.*, **37**, 1849–1858, <https://doi.org/10.1175/JPO3086.1>.
- , M. C. Gregg, and M. A. Merrifield, 2006: Structure, propagation, and mixing of energetic baroclinic tides in Mamala Bay, Oahu, Hawaii. *J. Phys. Oceanogr.*, **36**, 997–1018, <https://doi.org/10.1175/JPO2877.1>.
- Ansong, J. K., and Coauthors, 2017: Semidiurnal internal tide energy fluxes and their variability in a global ocean model and moored observations. *J. Geophys. Res. Oceans*, **122**, 1882–1900, <https://doi.org/10.1002/2016JC012184>.
- Armi, L., 1979: Effects of variations in eddy diffusivity on property distributions in the oceans. *J. Mar. Res.*, **37**, 515–530.
- Baines, P. G., 1998: *Topographic Effects in Stratified Flows*. Cambridge University Press, 482 pp.
- Becker, J., and Coauthors, 2009: Global bathymetry and elevation data at 30 arc seconds resolution: SRTM30_PLUS. *Mar. Geod.*, **32**, 355–371, <https://doi.org/10.1080/01490410903297766>.
- Bell, T., 1975a: Lee waves in stratified flows with simple harmonic time dependence. *J. Fluid Mech.*, **67**, 705–722, <https://doi.org/10.1017/S0022112075000560>.
- , 1975b: Topographically generated internal waves in the open ocean. *J. Geophys. Res.*, **80**, 320–327, <https://doi.org/10.1029/JC080i003p00320>.
- Dalcin, L., R. Paz, M. Storti, and J. D'Elia, 2008: MPI for Python: Performance improvements and MPI-2 extensions. *J. Parallel Distrib. Comput.*, **68**, 655–662, <https://doi.org/10.1016/j.jpdc.2007.09.005>.
- , —, P. Kler, and A. Cosimo, 2011: Parallel distributed computing using Python. *Adv. Water Resour.*, **34**, 1124–1139, <https://doi.org/10.1016/j.advwatres.2011.04.013>.
- de Lavergne, C., G. Madec, J. Le Sommer, A. G. Nurser, and A. C. Naveira Garabato, 2016: The impact of a variable mixing efficiency on the abyssal overturning. *J. Phys. Oceanogr.*, **46**, 663–681, <https://doi.org/10.1175/JPO-D-14-0259.1>.
- Desaubies, Y., and M. Gregg, 1981: Reversible and irreversible finestructure. *J. Phys. Oceanogr.*, **11**, 541–556, [https://doi.org/10.1175/1520-0485\(1981\)011<0541:RAIF>2.0.CO;2](https://doi.org/10.1175/1520-0485(1981)011<0541:RAIF>2.0.CO;2).
- Dunphy, M., A. L. Ponte, P. Klein, and S. Le Gentil, 2017: Low-mode internal tide propagation in a turbulent eddy field. *J. Phys. Oceanogr.*, **47**, 649–665, <https://doi.org/10.1175/JPO-D-16-0099.1>.
- Egbert, G. D., and R. D. Ray, 2000: Significant dissipation of tidal energy in the deep ocean inferred from satellite altimeter data. *Nature*, **405**, 775–778, <https://doi.org/10.1038/35015531>.
- , and —, 2001: Estimates of M_2 tidal energy dissipation from TOPEX/Poseidon altimeter data. *J. Geophys. Res.*, **106**, 22 475–22 502, <https://doi.org/10.1029/2000JC000699>.
- , and S. Y. Erofeeva, 2002: Efficient inverse modeling of barotropic ocean tides. *J. Atmos. Oceanic Technol.*, **19**, 183–204, [https://doi.org/10.1175/1520-0426\(2002\)019<0183:EIMOBO>2.0.CO;2](https://doi.org/10.1175/1520-0426(2002)019<0183:EIMOBO>2.0.CO;2).
- Falahat, S., J. Nycander, F. Roquet, A. M. Thurnherr, and T. Hibiya, 2014a: Comparison of calculated energy flux of internal tides with microstructure measurements. *Tellus*, **66A**, 23240, <https://doi.org/10.3402/tellusa.v66.23240>.
- , —, —, and M. Zarroug, 2014b: Global calculation of tidal energy conversion into vertical normal modes.

- J. Phys. Oceanogr.*, **44**, 3225–3244, <https://doi.org/10.1175/JPO-D-14-0002.1>.
- Garrett, C., and E. Kunze, 2007: Internal tide generation in the deep ocean. *Annu. Rev. Fluid Mech.*, **39**, 57–87, <https://doi.org/10.1146/annurev.fluid.39.050905.110227>.
- Gill, A. E., 1982: *Atmosphere–Ocean Dynamics*. Academic Press, 662 pp.
- Goff, J. A., 1991: A global and regional stochastic analysis of near-ridge abyssal hill morphology. *J. Geophys. Res.*, **96**, 21 713–21 737, <https://doi.org/10.1029/91JB02275>.
- Green, J. M., and J. Nylander, 2013: A comparison of tidal conversion parameterizations for tidal models. *J. Phys. Oceanogr.*, **43**, 104–119, <https://doi.org/10.1175/JPO-D-12-023.1>.
- Jayne, S. R., and L. C. St. Laurent, 2001: Parameterizing tidal dissipation over rough topography. *Geophys. Res. Lett.*, **28**, 811–814, <https://doi.org/10.1029/2000GL012044>.
- Kerry, C. G., B. S. Powell, and G. S. Carter, 2014: The impact of subtidal circulation on internal-tide-induced mixing in the Philippine Sea. *J. Phys. Oceanogr.*, **44**, 3209–3224, <https://doi.org/10.1175/JPO-D-13-0249.1>.
- Klymak, J. M., and Coauthors, 2006: An estimate of tidal energy lost to turbulence at the Hawaiian Ridge. *J. Phys. Oceanogr.*, **36**, 1148–1164, <https://doi.org/10.1175/JPO2885.1>.
- , R. Pinkel, and L. Rainville, 2008: Direct breaking of the internal tide near topography: Kaena Ridge, Hawaii. *J. Phys. Oceanogr.*, **38**, 380–399, <https://doi.org/10.1175/2007JPO3728.1>.
- Kunze, E., 2017: Internal-wave-driven mixing: Global geography and budgets. *J. Phys. Oceanogr.*, **47**, 1325–1345, <https://doi.org/10.1175/JPO-D-16-0141.1>.
- Ledwell, J., E. Montgomery, K. Polzin, L. St. Laurent, R. Schmitt, and J. Toole, 2000: Evidence for enhanced mixing over rough topography in the abyssal ocean. *Nature*, **403**, 179–182, <https://doi.org/10.1038/35003164>.
- Lefauve, A., C. Muller, and A. Melet, 2015: A three-dimensional map of tidal dissipation over abyssal hills. *J. Geophys. Res. Oceans*, **120**, 4760–4777, <https://doi.org/10.1002/2014JC010598>.
- Llewellyn Smith, S. G., and W. Young, 2002: Conversion of the barotropic tide. *J. Phys. Oceanogr.*, **32**, 1554–1566, [https://doi.org/10.1175/1520-0485\(2002\)032<1554:COTBT>2.0.CO;2](https://doi.org/10.1175/1520-0485(2002)032<1554:COTBT>2.0.CO;2).
- Locarnini, R., and Coauthors, 2013: *Temperature*. Vol. 1, *World Ocean Atlas 2013*, NOAA Atlas NESDIS 73, 40 pp., https://data.nodc.noaa.gov/woa/WOA13/DOC/woa13_voll.pdf.
- Lueck, R. G., and T. D. Mudge, 1997: Topographically induced mixing around a shallow seamount. *Science*, **276**, 1831–1833, <https://doi.org/10.1126/science.276.5320.1831>.
- MacKinnon, J. A., and Coauthors, 2017: Climate process team on internal wave–driven ocean mixing. *Bull. Amer. Meteor. Soc.*, **98**, 2429–2454, <https://doi.org/10.1175/BAMS-D-16-0030.1>.
- Mashayek, A., R. Ferrari, M. Nikurashin, and W. Peltier, 2015: Influence of enhanced abyssal diapycnal mixing on stratification and the ocean overturning circulation. *J. Phys. Oceanogr.*, **45**, 2580–2597, <https://doi.org/10.1175/JPO-D-15-0039.1>.
- Melet, A., M. Nikurashin, C. Muller, S. Falahat, J. Nylander, P. G. Timko, B. K. Arbic, and J. A. Goff, 2013: Internal tide generation by abyssal hills using analytical theory. *J. Geophys. Res. Oceans*, **118**, 6303–6318, <https://doi.org/10.1002/2013JC009212>.
- Merrifield, M. A., and P. E. Holloway, 2002: Model estimates of M_2 internal tide energetics at the Hawaiian Ridge. *J. Geophys. Res.*, **107**, 3179, <https://doi.org/10.1029/2001JC000996>.
- Munk, W., and C. Wunsch, 1998: Abyssal recipes II: Energetics of tidal and wind mixing. *Deep-Sea Res. I*, **45**, 1977–2010, [https://doi.org/10.1016/S0967-0637\(98\)00070-3](https://doi.org/10.1016/S0967-0637(98)00070-3).
- Nash, J. D., E. Kunze, J. M. Toole, and R. W. Schmitt, 2004: Internal tide reflection and turbulent mixing on the continental slope. *J. Phys. Oceanogr.*, **34**, 1117–1134, [https://doi.org/10.1175/1520-0485\(2004\)034<1117:ITRATM>2.0.CO;2](https://doi.org/10.1175/1520-0485(2004)034<1117:ITRATM>2.0.CO;2).
- , M. H. Alford, and E. Kunze, 2005: Estimating internal wave energy fluxes in the ocean. *J. Atmos. Oceanic Technol.*, **22**, 1551–1570, <https://doi.org/10.1175/JTECH1784.1>.
- , M. Alford, E. Kunze, K. Martini, and S. Kelly, 2007: Hotspots of deep ocean mixing on the Oregon continental slope. *Geophys. Res. Lett.*, **34**, L01605, <https://doi.org/10.1029/2006GL028170>.
- Nylander, J., 2005: Generation of internal waves in the deep ocean by tides. *J. Geophys. Res.*, **110**, C10028, <https://doi.org/10.1029/2004JC002487>.
- Oakey, N., 1982: Determination of the rate of dissipation of turbulent energy from simultaneous temperature and velocity shear microstructure measurements. *J. Phys. Oceanogr.*, **12**, 256–271, [https://doi.org/10.1175/1520-0485\(1982\)012<0256:DOTROD>2.0.CO;2](https://doi.org/10.1175/1520-0485(1982)012<0256:DOTROD>2.0.CO;2).
- Polzin, K., J. Toole, J. Ledwell, and R. Schmitt, 1997: Spatial variability of turbulent mixing in the abyssal ocean. *Science*, **276**, 93–96, <https://doi.org/10.1126/science.276.5309.93>.
- Rainville, L., and R. Pinkel, 2006: Propagation of low-mode internal waves through the ocean. *J. Phys. Oceanogr.*, **36**, 1220–1236, <https://doi.org/10.1175/JPO2889.1>.
- Ray, R. D., 1998: Ocean self-attraction and loading in numerical tidal models. *Mar. Geod.*, **21**, 181–192, <https://doi.org/10.1080/01490419809388134>.
- Rudnick, D. L., and Coauthors, 2003: From tides to mixing along the Hawaiian Ridge. *Science*, **301**, 355–357, <https://doi.org/10.1126/science.1085837>.
- Searle, R., 1987: Regional setting and geophysical characterization of the Great Meteor East area in the Madeira Abyssal Plain. *Geol. Soc. London Spec. Publ.*, **31**, 49–70, <https://doi.org/10.1144/GSL.SP.1987.031.01.06>.
- Sharples, J., 2016: RRS *James Clark Ross* 25th May–10th July 2016: RidgeMix NERC responsive mode project. University of Liverpool JR15-007 Cruise Rep., 104 pp., https://www.bodc.ac.uk/resources/inventories/cruise_inventory/reports/jr15007.pdf.
- Smith, W., and D. Sandwell, 1997: Global sea floor topography from satellite altimetry and ship depth soundings. *Science*, **277**, 1956–1962, <https://doi.org/10.1126/science.277.5334.1956>.
- St. Laurent, L., and C. Garrett, 2002: The role of internal tides in mixing the deep ocean. *J. Phys. Oceanogr.*, **32**, 2882–2899, [https://doi.org/10.1175/1520-0485\(2002\)032<2882:TROITI>2.0.CO;2](https://doi.org/10.1175/1520-0485(2002)032<2882:TROITI>2.0.CO;2).
- , and J. Nash, 2004: An examination of the radiative and dissipative properties of deep ocean internal tides. *Deep-Sea Res. II*, **51**, 3029–3042, <https://doi.org/10.1016/j.dsr2.2004.09.008>.
- , H. Simmons, and S. Jayne, 2002: Estimating tidally driven mixing in the deep ocean. *Geophys. Res. Lett.*, **29**, 2106, <https://doi.org/10.1029/2002GL015633>.
- Timko, P. G., B. K. Arbic, J. A. Goff, J. K. Ansong, W. H. Smith, A. Melet, and A. J. Wallcraft, 2017: Impact of synthetic abyssal hill roughness on resolved motions in numerical global ocean tide models. *Ocean Modell.*, **112**, 1–16, <https://doi.org/10.1016/j.ocemod.2017.02.005>.
- Wunsch, C., and R. Ferrari, 2004: Vertical mixing, energy, and the general circulation of the oceans. *Annu. Rev. Fluid Mech.*, **36**, 281–314, <https://doi.org/10.1146/annurev.fluid.36.050802.122121>.

- Zaron, E. D., and G. D. Egbert, 2014: Time-variable refraction of the internal tide at the Hawaiian Ridge. *J. Phys. Oceanogr.*, **44**, 538–557, <https://doi.org/10.1175/JPO-D-12-0238.1>.
- Zhao, Z., M. H. Alford, J. A. MacKinnon, and R. Pinkel, 2010: Long-range propagation of the semidiurnal internal tide from the Hawaiian Ridge. *J. Phys. Oceanogr.*, **40**, 713–736, <https://doi.org/10.1175/2009JPO4207.1>.
- , —, J. B. Girton, L. Rainville, and H. L. Simmons, 2016: Global observations of open-ocean mode-1 M_2 internal tides. *J. Phys. Oceanogr.*, **46**, 1657–1684, <https://doi.org/10.1175/JPO-D-15-0105.1>.
- Zilberman, N., J. Becker, M. Merrifield, and G. Carter, 2009: Model estimates of M_2 internal tide generation over Mid-Atlantic Ridge topography. *J. Phys. Oceanogr.*, **39**, 2635–2651, <https://doi.org/10.1175/2008JPO4136.1>.
- Zweng, M., and Coauthors, 2013: *Salinity*. Vol. 2, *World Ocean Atlas 2013*, NOAA Atlas NESDIS 74, 39 pp., https://data.noaa.gov/woa/WOA13/DOC/woa13_vol2.pdf.